

Emergent ferroelectricity in the two-dimensional Janus MoSSe monolayer driven by nondegenerate phonon instability

Zhi-Long Cao(曹智龙), Chen Cao(曹琛), Jia-Jun Xu(徐佳俊), Jia-Xu Yan(闫家旭), Lei Liu(刘雷), and De-Zhen Shen(申德振)

Citation: Chin. Phys. B, 2025, 34 (**11**): 117305. DOI: 10.1088/1674-1056/ae0d57
http://cpb.iphy.ac.cn; http://iopscience.iop.org/cpb

What follows is a list of articles you may be interested in

Semiregular tessellation of electronic lattices in untwisted bilayer graphene under anisotropic strain gradients

Zeyu Liu(刘泽宇), Xianghua Kong(孔祥华), Zhidan Li(李志聃), Zewen Wu(吴泽文), Linwei Zhou(周霖蔚), Cong Wang(王聪), and Wei Ji(季威)

Chin. Phys. B, 2025, 34 (**9**): 097309. DOI: 10.1088/1674-1056/adfb54

Doping-induced magnetic and topological transitions in $Mn_2X_2Te_5$ (X = Bi, Sb) bilayers

Wei Chen(陈威), Chuhan Tang(唐楚涵), Chao-Fei Liu(刘超飞), and Mingxing Chen(陈明星)

Chin. Phys. B, 2025, 34 (**9**): 097304. DOI: 10.1088/1674-1056/ade4af

Electronic structure and carrier mobility of BSb nanotubes

Lantian Xue(薛岚天), Chennan Song(宋晨楠), Miaomiao Jian(见苗苗), Qiang Xu(许强), Yuhao Fu(付钰豪), Pengyue Gao(高朋越), and Yu Xie(谢禹)

Chin. Phys. B, 2025, 34 (**3**): 037304. DOI: 10.1088/1674-1056/adacd3

Intrinsic valley-polarized quantum anomalous Hall effect in a two-dimensional germanene/MnI_2 van der Waals heterostructure

Xiao-Jing Dong(董晓晶) and Chang-Wen Zhang(张昌文)

Chin. Phys. B, 2024, 33 (**7**): 077303. DOI: 10.1088/1674-1056/ad4bbd

Optical second-harmonic generation of Janus MoSSe monolayer

Ce Bian(边策), Jianwei Shi(史建伟), Xinfeng Liu(刘新风), Yang Yang(杨洋), Haitao Yang(杨海涛), and Hongjun Gao(高鸿钧)

Chin. Phys. B, 2022, 31 (**9**): 097304. DOI: 10.1088/1674-1056/ac6db4

RAPID COMMUNICATION

Emergent ferroelectricity in the two-dimensional Janus MoSSe monolayer driven by nondegenerate phonon instability

Zhi-Long Cao(曹智龙)[1,2], Chen Cao(曹琛)[1,2], Jia-Jun Xu(徐佳俊)[1,2], Jia-Xu Yan(闫家旭)[1,2,†], Lei Liu(刘雷)[1,2], and De-Zhen Shen(申德振)[1,2]

[1] *State Key Laboratory of Luminescence Science and Technology, Changchun Institute of Optics, Fine Mechanics and Physics, Chinese Academy of Sciences, Changchun* 130033, *China*

[2] *University of Chinese Academy of Sciences, Beijing* 100049, *China*

(Received 16 July 2025; revised manuscript received 19 September 2025; accepted manuscript online 30 September 2025)

We report the discovery of bistable polar states with switchable polarization in the Janus monolayer 1T-MoSSe, induced by symmetry breaking in its chalcogen atomic layers. Our results demonstrate that Janus 1T-MoSSe exhibits two out-of-plane bistable polar states with switchable polarization, rather than polarization emerging from a non-polar phase, which represents an unconventional form of ferroelectric-like behavior. First-principles calculations and phenomenological modeling reveal that the inequivalent stacking of sulfur and selenium (S/Se) atoms breaks central inversion symmetry, activating non-degenerate phonon modes at the K-point (K_2/K_3) that drive the structural transformation between metastable d1T$_S$ and d1T$_{Se}$ phases. This coupling enables bipolar control of out-of-plane polarization through atomic displacements and charge redistribution, resulting in a polarization change of $\Delta P \approx \pm 0.3$ μC/cm^2. The Landau free energy analysis indicates that anharmonic terms and inter-mode coupling generate an asymmetric double-well potential, which is essential for the stabilization of bistable polar states. Molecular dynamics simulations show that the d1T$_S$ phase remains stable at high temperatures, whereas the d1T$_{Se}$ phase undergoes an irreversible phase transition near 300 K, accompanied by a Peierls-like distortion of the Mo atomic chain. This transition is driven by differences in electronegativity, atomic radius, and d–p orbital hybridization between S and Se. Our findings establish a theoretical framework for engineering nonlinear responses in two-dimensional (2D) ferroelectrics and suggest that low-energy polarization reversal at room temperature can be achieved through strain or electric-field control, offering promising opportunities for non-volatile memory and piezoelectric sensing applications.

Keywords: Janus MoSSe monolayer, ferroelectric phase transitions, first-principles calculations

PACS: 73.63.Bd, 77.80.B–, 63.20.dk

DOI: 10.1088/1674-1056/ae0d57 **CSTR:** 32038.14.CPB.ae0d57

1. Introduction

Two-dimensional (2D) ferroelectric (FE) materials, characterized by bistable polarization and reversible switching under external electric fields, have attracted considerable attention for their potential applications in miniaturized nanoelectronics.[1–4] However, conventional three-dimensional (3D) FE materials face severe challenges when scaled down, such as strong depolarization fields and surface effects, which hinder the stabilization of spontaneous polarization at the atomic scale.

In conventional FE systems, stable out-of-plane (OOP) polarization in ultrathin films is rare due to surface charge accumulation, which generates depolarization fields that suppress spontaneous polarization perpendicular to the surface. According to modern ferroelectricity theory, proper ferroelectricity arises from the condensation of polar optical phonons in a high-symmetry nonpolar phase.[5] However, the reduction in free energy associated with OOP polarization condensation is often insufficient to overcome the depolarization field.[6] Therefore, additional mechanisms beyond second-order lattice coupling are essential to stabilize OOP polarization in 2D FE materials. For instance, in 2D In_2Se_3, interlattice mode coupling beyond the P^2 term plays a crucial role in stabilizing the polarization.[7]

Various physical mechanisms have been explored in 2D FE materials, such as: (i) displacement-driven ferroelectricity: In $CuInP_2S_6$ thin films, spontaneous polarization is driven by the displacement of the copper sublattice away from the centrosymmetric position toward the indium sublattice.[8] Similarly, in SnTe thin films, a structural phase transition from the centrosymmetric rock-salt to the non-centrosymmetric orthorhombic γ phase results in substantial in-plane ionic displacements, inducing spontaneous polarization.[9] In α-In_2Se_3, subtle displacements of Se ions, coupled with in-plane distortions, generate spontaneous polarization and enable dipole locking and polarization reversibility.[10–13] (ii) Sliding ferroelectricity: In 2D van der Waals bilayer systems such as 1T′-WTe_2[14–16] and 1T′-$PtTe_2$ π bilayers,[17] inter-

†Corresponding author. E-mail: yanjiaxu@ciomp.ac.cn

© 2025 Chinese Physical Society and IOP Publishing Ltd. All rights, including for text and data mining, AI training, and similar technologies, are reserved.

layer sliding-induced displacements break crystal symmetry, leading to reversible vertical polarization. (iii) Hybrid improper ferroelectricity: In distorted 1T-phase transition-metal chalcogenides such as MoS_2[18,19] and $MoTe_2$,[20,21] mixed improper polarization arises from nonlinear coupling between polar modes and nonpolar order parameters. This complex behavior requires synchronization of multiple excitations for polarization switching, resulting in multi-mode effects and intricate phase-transition barriers. These advancements have propelled research on 2D ferroelectric materials, broadening our understanding of ferroelectric phenomena across diverse systems.

Two-dimensional Janus monolayers, characterized by mirror asymmetry, represent a promising class of materials with unique physical properties. Graphone (single-sided hydrogenated graphene) was the first proposed 2D Janus material.[22] Since then, the synthesis of Janus structures has drawn extensive attention owing to their potential applications in separation membranes, electronics, and spintronics.[23–26] Typically, these materials are synthesized via bottom-up approaches, such as selective chemical functionalization or surface-layer element substitution in transition-metal dichalcogenides (TMDs).[27,28] Janus materials exhibit distinctive features, including the Rashba effect,[29] valley spin splitting,[30,31] enhanced catalytic activity,[32,33] and piezoelectricity.[34,35]

Recently, Janus TMD structures have been fabricated by selectively replacing chalcogen atoms in monolayer TMDs (e.g., 1H-MoS_2). Most synthesized Janus TMDs adopt the semiconducting 1H-phase; however, a metastable 1T′-MoSSe phase has also been synthesized as a core–shell structure encapsulated on Au nanoparticles, which demonstrated superior electrocatalytic hydrogen evolution reaction (HER) activity.[36] These Janus TMD monolayers MXY ($M = \mathrm{Mo, W}$; $X \neq Y = \mathrm{S, Se, Te}$) possess an intrinsic dipole moment due to broken mirror symmetry and exhibit pronounced Rashba and valley spin splitting, which could strongly impact spintronic and valleytronic applications.[37] Among these, MoSSe monolayers,[28] derived from MoS_2 by substituting sulfur with selenium, have shown great promise as efficient photocatalysts for solar-driven water splitting owing to their low carrier recombination rates.[38] Additionally, the Janus VSSe monolayer, exhibiting both piezoelectricity and ferroelasticity, holds potential for applications in nanoelectronics, optoelectronics, and valleytronics.[39]

Despite this remarkable progress, an open question remains as to whether Janus TMDs can exhibit reversible polarization phase transitions analogous to those in conventional ferroelectrics. Conventional 1H-MoSSe is polar but non-ferroelectric,[28] yet the recent synthesis of metastable 1T′-MoSSe[36] hints at an unconventional type of ferroelectricity reminiscent of sliding ferroelectricity in other reconstructed TMDs (e.g., 1T′-WTe_2 bilayers[14–16]). Consistent with theoretical predictions, reconstructed TMD systems can exhibit intrinsic ferroelectricity; this has been experimentally confirmed in other reconstructed phases such as d1T-$MoTe_2$[20] and 1T″-MoS_2,[40] where structural trimerization leads to bistable polarization states.

In this work, we uncover the bistable ferroelectric characteristics induced by symmetry breaking and elucidate their microscopic mechanisms in the Janus monolayer 1T-MoSSe through a multiscale theoretical framework combining first-principles calculations, molecular dynamics simulations, and a phenomenological Landau model. Specifically, the inequivalent stacking of S and Se atoms in the chalcogen layers breaks the inversion symmetry of the system, thereby activating non-degenerate K_2/K_3 phonon modes at the K point. These phonon modes drive the structural reconstruction of metastable $\mathrm{d1T_S}$ and $\mathrm{d1T_{Se}}$ phases, enabling bipolar control of out-of-plane polarization through cooperative chalcogen displacements and charge redistribution. The Landau free energy model constructed from symmetry analysis reveals that third-order anharmonic terms and repulsive inter-mode coupling generate an asymmetric double-well potential, which is key to achieving bistable ferroelectricity. Molecular dynamics simulations further uncover thermodynamic competition between metastable phases: the $\mathrm{d1T_S}$ phase remains stable with polarization at elevated temperatures, whereas the $\mathrm{d1T_{Se}}$ phase undergoes an irreversible phase transition near room temperature, accompanied by a Peierls-like distortion of the Mo atomic chain and polarization switching. This transition is primarily attributed to differences in electronegativity, atomic radius, and d–p orbital hybridization between S and Se, which significantly modulate bond lengths and binding energies. Finally, we construct a polarization expansion model based on the displacement dependence of chalcogen atoms, providing a theoretical framework for controlling the nonlinear response of 2D ferroelectrics. Our findings suggest that by tuning strain or electric-field-driven competition between the K_2 and K_3 modes, low-energy polarization reversal at room temperature can be achieved, offering a promising pathway for non-volatile memory and piezoelectric device applications.

2. Method

All calculations were carried out within the framework of density functional theory (DFT) using the Vienna *Ab-initio* simulation package (VASP).[41,42] The exchange-correlation interactions between electrons were treated with the Perdew–Burke–Ernzerhof (PBE) parameterization of the generalized gradient approximation (GGA).[43–45] A $12 \times 12 \times 1$ k-point mesh (consistent with the Brillouin-zone sampling of subsequent supercells) and a plane-wave cutoff energy of 550 eV

were employed. The projector augmented wave (PAW) method was used to describe ion–electron interactions, with explicit treatment of valence electrons for Mo ($4p^6 4d^5 5s^1$), S ($3s^2 3p^4$), and Se ($4s^2 4p^4$). All geometries were fully relaxed until atomic forces were below 10^{-2} eV/Å, and the convergence criterion for electronic self-consistent iterations was set to 10^{-7} eV. A vacuum layer of at least 10 Å was added to avoid spurious interlayer interactions under periodic boundary conditions.

The transformation pathway and energy barriers between 1T and d1T phases were calculated using the nudged elastic band (NEB) method.[46,47] Phonon spectra were obtained via density functional perturbation theory using the PHONOPY code.[48–50] Electric polarization was computed using the charge-center method. Group-theoretical analysis of order parameters was performed using the ISOTROPY package.[51]

The temperature dependence of polarization was examined via machine-learning-accelerated *ab initio* molecular dynamics (AIMD) simulations on $3 \times 3 \times 1$ supercells. Machine-learning-force-field-enhanced VASP simulations were conducted in the NVT ensemble using the Nosé–Hoover thermostat.[52] For each temperature, 5000-step AIMD simulations were performed with a 1 fs timestep. Polarization–temperature relationships were derived by analyzing atomic displacement parameters and calculating effective charges via the Berry-phase method.

3. Results and discussions

3.1. Symmetry breaking induced metastable polarization structures

The monolayer Janus 1T-MoSSe adopts a hexagonal crystal structure (space group $P3m1$, No. 156), as shown in Fig. 1(a). The molybdenum (Mo) atomic layer is asymmetrically sandwiched between the upper selenium (Se) and lower sulfur (S) atomic layers, forming an ABC stacking sequence. Each Mo atom is coordinated by three Se atoms from the upper layer and three S atoms from the lower layer, forming a $[MoSe_3S_3]$ octahedral coordination that induces an intrinsic out-of-plane electric dipole moment of 1.437 μC/cm^2, thus breaking the centrosymmetry of the conventional 1T-MoX_2 (X = S, Se, Te) phase (space group $P\bar{3}m1$, No. 164). Our calculations yield a lattice constant of 3.19 Å for the 1T-phase unit cell $p(1 \times 1)$, with the boundary of the $p(\sqrt{3} \times \sqrt{3})$ supercell indicated by the dashed box in Fig. 1(a).

Group-theoretical analysis indicates that when the $P3m1$ (No. 156) symmetry evolves into the $P31m$ (No. 157) phase, two types of lattice instability modes emerge (Fig. 1(b)), revealing the metastable nature of 1T-MoSSe. The K-point phonon modes K_2 and K_3 (belonging to the K irreducible representation) dominate the structural distortion: the in-plane shear motion of Mo atoms couples with the asymmetric displacements of the upper and lower chalcogen atoms, forming two distinct phase-transition pathways. It is worth noting that, since the parent $P3m1$ phase already lacks spatial inversion symmetry, there is no longer a symmetry relation between the K_2 and K_3 modes. This non-degeneracy can be understood from the viewpoint of subgroup relations: the doubly degenerate K-point representation of the centrosymmetric parent group $P\bar{3}m1$ (No. 164) splits into two distinct one-dimensional representations in the lower-symmetry Janus group $P3m1$, thereby lifting the original degeneracy. Lattice-dynamics calculations reveal that the relaxed d1T$_S$ (lattice constant 5.71 Å) and d1T$_{Se}$ (5.73 Å) phases both undergo pronounced structural reconstruction.

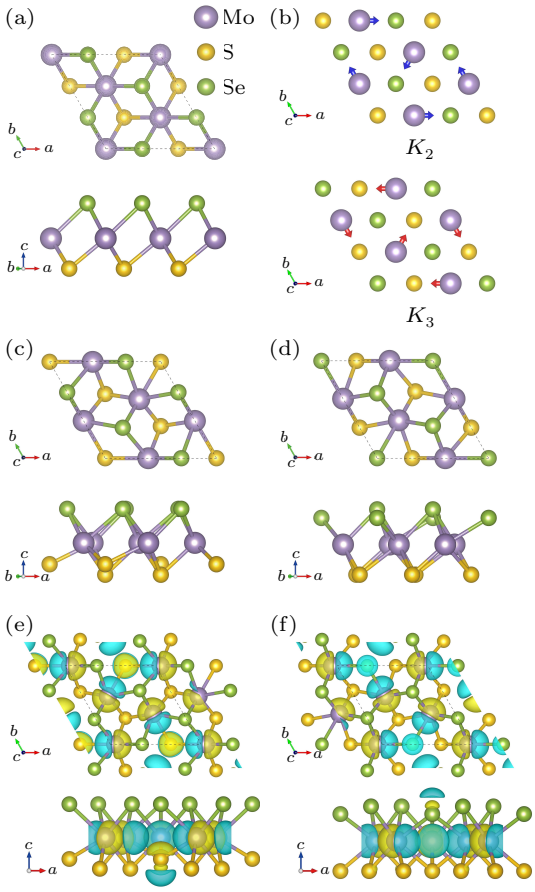


Fig. 1. Schematic diagram of atomic structures and studied phonon modes in a $p(\sqrt{3} \times \sqrt{3})$ supercell. (a) The 1T-phase of MoSSe, with the $p(1 \times 1)$ formula unit cell indicated by a dashed line. Purple atoms represent molybdenum, yellow atoms represent sulfur in the lower layer, and green atoms represent selenium in the uppper layer. (b) Vibrational modes of the 1T-phase, with eigenvectors indicated by arrows for the K_2 and K_3 modes. (c) Top and side views of the atomic structure of the d1T$_S$-phase. (d) Top and side views of the atomic structure of the d1T$_{Se}$-phase. (e) Top and side views of the charge density difference between ferroelectric d1T$_S$-phase and non-ferroelectric 1T-phase. The yellow isosurface represents negative charge, and the cyan isosurface represents positive charge. (f) Top and side views of the charge density difference between ferroelectric d1T$_{Se}$-phase and non-ferroelectric 1T-phase.

According to the results of the vibrational mode decomposition (Table 1), the K_2 and K_3 modes predominantly govern the structural reconstruction processes of the d1T$_S$ and d1T$_{Se}$

phases, respectively. As shown in Fig. 1(c), the formation of the d1T$_S$ phase is mainly driven by the K_2 mode, which reconstructs the dominant structural evolution through the planar rotation of Mo trimers around the lower sulfur atoms. In contrast, the structural evolution of the d1T$_{Se}$ phase (see Fig. 1(d)) is primarily governed by the K_3 mode, which induces in-plane rotational motion of Mo trimers around the upper selenium atoms. It is worth noting that although the contribution of the Γ mode is significantly smaller than that of the dominant K modes, it exhibits element-dependent out-of-plane motion in both systems: sulfur atoms in the d1T$_S$ phase primarily undergo vertical displacement, whereas selenium atoms in the d1T$_{Se}$ phase move in the opposite direction, implying a reversal of the polarization vector during the structural phase transition.

To validate the above group-theoretical predictions, we computed the phonon dispersion relations of the 1T phase using first-principles calculations (Fig. 2(a)), where the high-symmetry points in the Brillouin zone are chosen as $\Gamma(0,0,0)$, $M(0.5,0,0)$, and $K(\frac{1}{3},\frac{1}{3},0)$. The results show that the system exhibits imaginary (negative) phonon frequencies at both the M and K points, directly reflecting the metastable nature of the 1T phase. Specifically, the lattice instability at the M point corresponds to a symmetry-breaking transition from 1T to 1T′, while the two non-degenerate imaginary-frequency modes at the K point (K_2 and K_3) correspond to the distortion modes identified in the group-theoretical analysis. Notably, since the $P3m1$ space group already lacks spatial inversion symmetry, the K_2 and K_3 modes belong to different irreducible representations, in contrast to the degenerate K-point phonons in the centrosymmetric 1T phase (space group $P\bar{3}m1$).

Although the 1T-MoSSe monolayer formally belongs to the $P3m1$ space group and thus lacks inversion symmetry, the chemical and structural similarities between the S and Se layers produce an approximate higher (pseudo-centrosymmetric) symmetry. As a result, the two distinct K-point soft modes remain nearly degenerate, manifesting as a broad imaginary band in Fig. 2(a). This near-degeneracy, arising from pseudo-symmetry, also explains why the two distorted phases (d1T$_S$ and d1T$_{Se}$) possess comparable energies. The phonon analysis is further supported by the vibrational mode decomposition in Table 1, which clearly reveals that the K_2 and K_3 modes respectively dominate the structural reconstruction mechanisms of the d1T$_S$ and d1T$_{Se}$ phases.

Table 1. The projected amplitudes of each phonon mode in the distortions from the 1T-phase to the d1T$_S$- and d1T$_{Se}$-phase. For each distortion the total atomic-displacement amplitude is normalized to 100%.

d1T$_S$		d1T$_{Se}$	
Mode	Amplitude	Mode	Amplitude
Γ_1	7.67%	Γ_1	11.81%
K_2	92.33%	K_2	0.00%
K_3	0.00%	K_3	88.19%

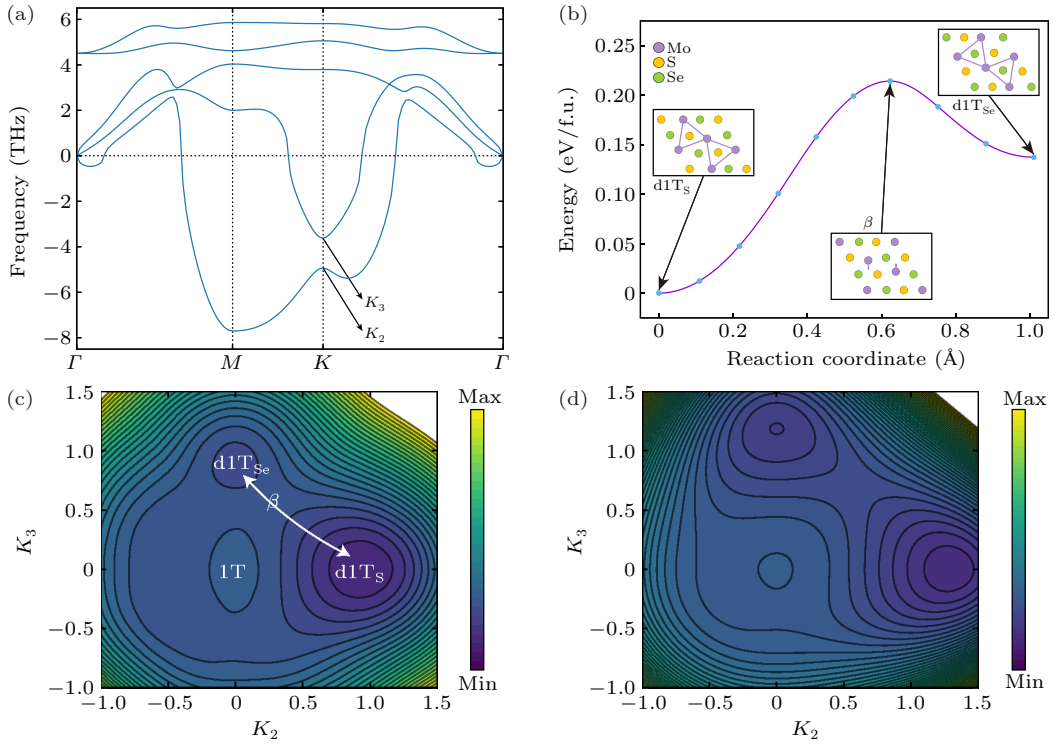


Fig. 2. (a) Phonon dispersion curves of the non-ferroelectric 1T-phase of monolayer MoSSe, with frequencies of unstable modes plotted as negative values. The selected high-symmetry points in the Brillouin zone are $\Gamma(0,0,0)$, $M(0.5,0,0)$, and $K(\frac{1}{3},\frac{1}{3},0)$. (b) Transition pathway between the d1T$_S$- and d1T$_{Se}$-phases, with the transition state and corresponding characteristic structures highlighted. (c) Contour diagram of the potential energy surface (PES) calculated from first-principles calculations, projected onto the $\{K_2,K_3\}$ subspace. Color depth indicates the total lattice free energy. (d) PES projected onto the $\{K_2,K_3\}$ subspace, as described by the phenomenological model referring to Eq. (1) in the main text. Color depth indicates the total system energy.

The charge density difference analysis (Figs. 1(e) and 1(f)) further reveals the microscopic mechanism of symmetry breaking. In the d1T_S phase, charge redistribution mainly occurs around the lower sulfur atom sites (yellow isosurfaces indicate electron accumulation, while cyan ones indicate electron depletion), whereas the d1T_{Se} phase exhibits an inverse charge-transfer feature localized at the upper selenium atoms. This localized charge reconstruction directly correlates with the displacement direction of the chalcogen atoms, driven by the K_2/K_3 and Γ vibrational modes. When sulfur atoms displace outward along the out-of-plane direction, their p_z orbital electrons migrate toward the lower layer; conversely, the negative displacement of selenium atoms leads to electron accumulation in the upper layer. The reversal of the charge-transfer direction ultimately causes a flip in the polarization orientation of the two distorted phases.

Quantitative calculations of the valence-electron charge center and ionic dipole contributions show that the out-of-plane polarization strengths of the d1T_S and d1T_{Se} phases are 1.817 μC/cm^2 and 1.223 μC/cm^2, respectively. These correspond to significant shifts of +0.38 μC/cm^2 and −0.21 μC/cm^2 relative to the 1T reference phase (1.437 μC/cm^2). This bipolar regulation feature arises from the dual-control mechanism of the K_2/K_3 and Γ modes over structural symmetry: when the chalcogen atoms displace in opposite directions, the resulting electron redistribution selectively enhances or weakens the intrinsic polarization field. These results systematically elucidate the structure–function relationship between symmetry breaking and polarization response. The K_2/K_3 and Γ modes jointly dictate the displacement direction of chalcogen atoms, determining not only the spatial pattern of charge transfer but also enabling reversible control over both the magnitude and direction of the ferroelectric polarization.

To preliminarily examine the thermodynamic stability of the distorted phases, we compared their relative free energies (Table 2). By fixing the 1T-phase lattice constant to eliminate strain effects, we found that the total energy of the 1T′ phase is 0.09 eV/f.u. lower than that of the d1T_{Se} phase, suggesting superior thermal stability of the former. However, the energy of the 1T phase, as a transition state, is 0.14 eV/f.u. higher than that of the d1T_{Se} phase, indicating that the transition from d1T_{Se} to 1T′ must overcome a considerable energy barrier — consistent with the metastable nature of the d1T_{Se} phase at low temperatures. In contrast, the d1T_S phase exhibits better thermal stability, with a free energy 0.28 eV/f.u. lower than that of the 1T phase. When lattice relaxation is allowed (right column of Table 2), the energy of each distorted phase decreases further, and the competition between the d1T_S and 1T′ phases suggests that the system may achieve multistable switching through stress or temperature field control.

Table 2. The relative energy values of different structures referring to 1T-phase (units: eV/f.u.).

Structure	Fixed lattice (eV/f.u.)	Relaxed lattice (eV/f.u.)
1T	0.000	0.000
d1T_S	−0.280	−0.322
d1T_{Se}	−0.143	−0.195
1T′	−0.231	−0.309
1H	−0.732	−0.739

The structural distortions of the 1T and d1T phases can be classified into two fundamental modes. The first is an out-of-plane collective displacement mode, in which the S and Se atoms on both sides move cooperatively along the out-of-plane direction. The lattice vibration of this mode corresponds to the phonon mode at the center of the Brillouin zone (the Γ point) without supercell modulation. Although this mode further breaks spatial inversion symmetry, the out-of-plane dipole moments of the S and Se atoms moving toward the central Mo layer tend to cancel each other, resulting in a weak or even reduced overall polarization effect.

The second mode is a supercell modulation mode associated with the irreducible representations K_2 and K_3 at the K point of the Brillouin zone (as shown in Fig. 1(b)). In the K_2 distortion, Mo atoms undergo in-plane trimerization, accompanied by in-plane trimerization of the upper Se atoms and pronounced out-of-plane displacement of the lower S atoms. In contrast, the K_3 distortion involves in-plane trimerization of Mo and lower S atoms, while the upper Se atoms exhibit out-of-plane displacement.

To explore possible polarization switching pathways, we calculated the transition state between the d1T_S and d1T_{Se} phases using the nudged elastic band (NEB) method (Fig. 2(b)). The results show that the lowest-energy transition pathway does not pass through the 1T phase but proceeds via a finite-amplitude β mode (a superposition of K_2 and K_3) as the transition state. The energy of this transition state is about 0.21 eV/f.u. higher than that of the d1T_S phase and 0.07 eV/f.u. higher than that of the d1T_{Se} phase, indicating that polarization switching requires overcoming an energy barrier on the order of 0.1 eV/f.u.

Furthermore, Fig. 2(c) shows the potential energy surface (PES) mapped on the K_2–K_3 mode subspace. Two nondegenerate energy minima appear, corresponding respectively to the distortions with $K_2 = 1$ and $K_3 = 1$. Notably, in conventional 1T-phase TMDs such as $MoTe_2$, the preservation of spatial inversion symmetry ensures that the K_2 and K_3 modes remain degenerate, resulting in a doubly degenerate ground state on the PES.[18,21] In contrast, in Janus-type MoSSe, the S/Se heterolayer breaks spatial inversion symmetry, causing the K_2 and K_3 modes to belong to different irreducible representations (Table 1), which lifts the degeneracy and leads to an energy splitting between the PES minima. This feature is also reflected in the nondegeneracy of the imaginary phonon

frequencies at the K point (Fig. 2(a)), where the K_2 mode exhibits a larger imaginary frequency, implying a stronger tendency toward lattice instability.

Owing to the hexagonal lattice symmetry, the $\{K_2, K_3\}$ subspace must respect threefold rotational operations, implying that a complete description requires introducing the three symmetry-equivalent sets of modes $\{K_2^i, K_3^i\}$ $(i = 1,2,3)$. Within each subspace, two nondegenerate minima exist, corresponding to forward (K_2^i-dominated) and reverse (K_3^i-dominated) out-of-plane polarizations with respect to the 1T reference phase. Moreover, the threefold degeneracy of the β mode indicates that the lattice can undergo polarization switching between the d1T phases through three symmetry-equivalent pathways, leading to multidomain polarization reversal behavior.

3.2. Phenomenological model of free-energy expansion

To gain deeper insight into the microscopic origin of the ferroelectric bistability in Janus monolayer MoSSe driven by the K_2/K_3 lattice modes, we construct a Landau-type phenomenological framework from the viewpoint of symmetry breaking. Considering the constraints imposed by the threefold rotational symmetry on atomic displacement patterns, together with the loss of spatial inversion symmetry in the Janus structure, the order parameter must simultaneously capture the nondegenerate contributions of both K_2 and K_3 modes. Therefore, the system's order parameter is described by the displacement amplitudes Q_{K_2} and Q_{K_3} within the $\{K_2, K_3\}$ subspace.

Symmetry analysis indicates that this subspace allows the presence of cubic anharmonic terms, from which the free-energy functional can be expressed as

$$\begin{aligned}\mathcal{F}(Q_{K_2}, Q_{K_3}) = {} & \alpha_1 Q_{K_2}^2 + \alpha_2 Q_{K_3}^2 + \beta_1 Q_{K_2}^3 + \beta_2 Q_{K_3}^3 \\ & + \gamma_1 Q_{K_2}^4 + \gamma_2 Q_{K_3}^4 + \delta Q_{K_2}^2 Q_{K_3}^2, \end{aligned} \tag{1}$$

where α_i, β_i, and γ_i $(i = 1,2)$ are expansion coefficients representing harmonic, cubic, and quartic contributions, respectively, and δ characterizes the coupling between the two modes.

The free-energy expansion in Eq. (1) captures the essential characteristics of the 1T $\rightarrow$ d1T phase transition. The interplay between the independent mode terms and the coupling term produces an inherently asymmetric double-well potential energy surface. Unlike conventional ferroelectrics constrained by inversion symmetry, the broken centrosymmetry of the Janus structure (space group $P31m$, No. 157) gives rise to nonzero cubic coefficients β_1 and β_2 (see Table 3). These nonvanishing cubic terms lead directly to an asymmetric double-well profile of the free-energy surface, as illustrated in Figs. 2(c) and 2(d). The comparable magnitudes of the quadratic and cubic terms further enhance the potential asymmetry, revealing the intrinsic first-order nature of the phase transition in this system.

Table 3. The value of each coefficient parameter in the Landau model of Eq. (1) in the absence of strain.

Coefficient	Value
α_1	−0.452
α_2	−0.344
β_1	−0.475
β_2	−0.421
γ_1	0.409
γ_2	0.388
δ	1.206

The second-order coefficients α_1 and α_2 are both negative, indicating that the K_2 and K_3 modes exhibit phonon instabilities with imaginary frequencies. The magnitude of α_1 is significantly larger than that of α_2, consistent with the stronger imaginary frequency feature of the K_2 mode observed in Fig. 2(a). This difference in instability implies that the two modes play distinct roles in structural distortion: the distortion dominated by the K_2 mode more readily drives the system into a low-energy configuration.

The positive coefficient of the inter-mode coupling term, $\delta Q_{K_2}^2 Q_{K_3}^2$ $(\delta > 0)$, reflects a mutual exclusion mechanism between the two displacement modes. When one mode is activated (e.g., $Q_{K_2} \neq 0$), the coupling term significantly raises the potential energy associated with the other mode, enforcing a single-mode ground state (either the d1T$_S$- or d1T$_{Se}$-phase). This competitive relationship is visually evident from the steep energy increase along the diagonal direction in Figs. 2(c) and 2(d), providing a mechanistic explanation for the formation of the bistable state.

Although the Landau free-energy expansion in Eq. (1) is truncated at the fourth-order term, it successfully reproduces the qualitative features of the potential energy surface obtained from first-principles calculations (see comparison in Figs. 2(c) and 2(d)). The deeper potential well associated with the K_2 mode ($\beta_1 < \beta_2$) aligns with the lower ground-state energy of the d1T$_S$-phase from NEB calculations, confirming that the cubic terms of the K_2^3 and K_3^3 modes, through lattice energy preferences, dominate the emergence and stability of switchable ferroelectric phases.

3.3. Phenomenological model of polarization expansion

To investigate the microscopic origins of polarization, we first focus on the coupling effects of the in-plane vibrational modes of Mo atoms on the out-of-plane polarization. Based on symmetry considerations and perturbation theory, the polarization along the z-direction, P_z, can be expressed as a series expansion in terms of the normal mode coordinates $Q_{K_2^{\mathrm{Mo}}}$ and $Q_{K_3^{\mathrm{Mo}}}$

$$\begin{aligned}P_z(Q_{K_2^{\mathrm{Mo}}}, Q_{K_3^{\mathrm{Mo}}}) = {} & P_0^{\mathrm{Janus}} + a_2 Q_{K_2^{\mathrm{Mo}}} + a_3 Q_{K_3^{\mathrm{Mo}}} \\ & + b_2 Q_{K_2^{\mathrm{Mo}}}^2 + b_3 Q_{K_3^{\mathrm{Mo}}}^2 + c_2 Q_{K_2^{\mathrm{Mo}}}^3 \\ & + c_3 Q_{K_3^{\mathrm{Mo}}}^3 + d_2 Q_{K_2^{\mathrm{Mo}}}^4 + d_3 Q_{K_3^{\mathrm{Mo}}}^4. \end{aligned} \tag{2}$$

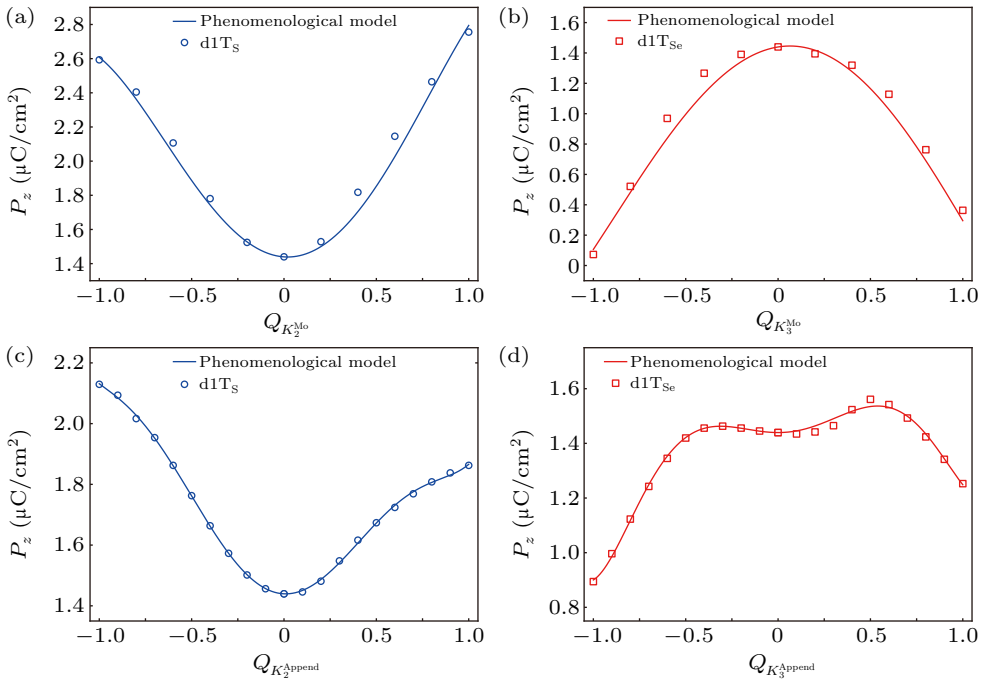


Fig. 3. (a) Evolution of polarization with respect to K_2^{Mo} distortion. The blue curve represents the analytic form from Eq. (2), and the blue symbols denote DFT data. (b) Evolution of polarization with respect to K_3^{Mo} distortion. The red curve represents the analytic form from Eq. (2), and the red symbols denote DFT data. (c) Evolution of polarization with respect to K_2 distortion. The blue curve represents the analytic form from Eq. (5), and the blue symbols denote DFT data. (d) Evolution of polarization with respect to K_3 distortion. The red curve represents the analytic form from Eq. (5), and the red symbols denote DFT data. Note that an effective monolayer thickness of 5 Å was used for the polarization calculation.

Table 4. The value of each coefficient parameter in the phenomenological model of Eq. (2) in the absence of strain.

Coefficient	Value
a_2	−0.075623
a_3	0.193778
b_2	1.875218
b_3	−1.501096
c_2	0.168827
c_3	−0.099192
d_2	−0.613514
d_3	0.262199

In the formula, P_0^{Janus} describes the intrinsic spontaneous polarization in the 1T-phase MoSSe Janus system with $P3m1$ (No. 156) space group, arising from the broken inversion symmetry. Figures 3(a) and 3(b) validate the reliability of this model through first-principles calculations, where the computed polarization values for the metastable configurations of d1T$_S$ and d1T$_{Se}$ are in high agreement with the model predictions.

Specifically, Table 4 shows that the secondary-term coefficients b_2 and b_3 differ significantly in magnitude and have opposite signs, indicating that the out-of-plane polarization P_z is primarily governed by these quadratic terms, while contributions from higher-order terms are relatively weak. This nonlinear behavior is evident in the variation of P_z with phonon mode coordinates $Q_{K_2^{Mo}}$ and $Q_{K_3^{Mo}}$: for the K_2^{Mo} mode, $P_z(Q_{K_2^{Mo}})$ shows a minimum at the origin and increases monotonically with positive curvature ($b_2 > 0$); in contrast, the K_3^{Mo} mode exhibits negative curvature ($b_3 < 0$), with $P_z(Q_{K_3^{Mo}})$ reaching a maximum at the origin and decreasing as the amplitude grows.

The opposite response of P_z to $Q_{K_2^{Mo}}$ and $Q_{K_3^{Mo}}$ originates from the distinct characteristics of the chalcogen atoms in the upper and lower layers. Specifically, the in-plane rotational motion of the Mo trimer driven by the K_2^{Mo} mode around the lower S atoms enhances the asymmetry of Mo–Se and Mo–S bonds, amplifying the intrinsic dipole moment. Conversely, the K_3^{Mo} mode reconfigures the Se/S charge transfer path, reducing the asymmetry of the original charge distribution and partially canceling the polarization vector. Additionally, differences in electronegativity between S and Se further modulate this nonlinear response, with higher electronegativity of S atoms facilitating stronger charge capture upon bond compression. This geometric-electronic coupling underlies the polarization enhancement (d1T$_S$-phase) and polarization decay (d1T$_{Se}$-phase), leading to two distinct metastable configurations in the potential well.

To quantify this effect, we extend the phenomenological model to include higher-order terms. The out-of-plane polarization P_z can then be expressed as a series expansion of the Mo atom K-point phonon modes and the cooperative displacement modes of the chalcogen atoms. Using group theoretical analysis and orthogonal decomposition, the system's displacement modes can be written in composite form

$$K_i^{Full} = K_i^{Mo} + \lambda_{\parallel} K_i^{Ch,\parallel} + \lambda_{\perp} K_i^{Ch,\perp}, \quad (3)$$
$$K_i^{Append} = K_i^{Full} + \gamma \Gamma_1^{Ch,\perp}$$

$$= K_i^{\mathrm{Mo}} + \lambda_{\parallel} K_i^{\mathrm{Ch},\parallel} + \lambda_{\perp} K_i^{\mathrm{Ch},\perp} + \gamma \Gamma_1^{\mathrm{Ch},\perp}. \quad (4)$$

Here, $K_i^{\mathrm{Ch},\parallel}$ represents the in-plane cooperative mode of the chalcogen atoms (maintaining C_3 symmetry), $K_i^{\mathrm{Ch},\perp}$ represents the out-of-plane anti-symmetric displacement mode, and $\Gamma_1^{\mathrm{Ch},\perp}$ characterizes the overall out-of-plane displacement of the chalcogen layer. The coupling coefficients $\lambda_{\parallel}$, $\lambda_{\perp}$, and γ are fixed at 1 after energy minimization to emphasize the cooperative effects.

For instance, in the d1T$_{\mathrm{S}}$-phase, the K_2^{Append} mode features an in-plane component $K_2^{\mathrm{Ch},\parallel}$ corresponding to Se trimer rotation synchronized with the Mo trimer, and an out-of-plane component $K_2^{\mathrm{Ch},\perp}$ where a single S atom moves positively along z while the other two move oppositely. The $\Gamma_1^{\mathrm{Ch},\perp}$ mode drives Se atoms toward the Mo layer and S atoms in the opposite direction (see Fig. 1(c)). This composite mode accurately reconstructs the lattice characteristics of the d1T$_{\mathrm{S}}$-phase (lattice constant 5.71 Å). Similarly, the K_3^{Append} mode, with Se and S roles swapped, produces the d1T$_{\mathrm{Se}}$-phase (5.73 Å).

The composite model K_i^{Append} incorporates the out-of-plane polarization directly induced by the in-plane displacement of Mo atoms, the nonlinear polarization from the cooperative displacement of chalcogen atoms in both in-plane and out-of-plane directions, and higher-order contributions from pure out-of-plane displacement. To accurately characterize these synergistic effects, the polarization strength model is extended to an expanded form that includes sixth-order nonlinear terms

$$\begin{aligned} & P_z\left(Q_{K_2^{\mathrm{Append}}}, Q_{K_3^{\mathrm{Append}}}\right) \\ = \; & P_0^{\mathrm{Janus}} + a_2 Q_{K_2^{\mathrm{Append}}} + a_3 Q_{K_3^{\mathrm{Append}}} + b_2 Q^2_{K_2^{\mathrm{Append}}} \\ & + b_3 Q^2_{K_3^{\mathrm{Append}}} + c_2 Q^3_{K_2^{\mathrm{Append}}} + c_3 Q^3_{K_3^{\mathrm{Append}}} + d_2 Q^4_{K_2^{\mathrm{Append}}} \\ & + d_3 Q^4_{K_3^{\mathrm{Append}}} + e_2 Q^5_{K_2^{\mathrm{Append}}} + e_3 Q^5_{K_3^{\mathrm{Append}}} + f_2 Q^6_{K_2^{\mathrm{Append}}} \\ & + f_3 Q^6_{K_3^{\mathrm{Append}}}. \end{aligned} \quad (5)$$

Figures 3(c) and 3(d) show the evolution of polarization intensity P_z with respect to the composite displacement modes $Q_{K_2^{\mathrm{Append}}}$ and $Q_{K_3^{\mathrm{Append}}}$. The excellent agreement between the model curves and DFT data validates the reasonableness of this extended model.

For the K_2^{Append} mode (Fig. 3(c)), P_z exhibits significant nonlinear growth. The positive curvature dominated by the quadratic coefficient b_2 (Table 5) indicates that the in-plane rotation of the Mo trimer enhances the polarization, consistent with previous results. The negative quartic term d_2 exerts a suppressive effect at large displacements ($|Q| > 0.8$), leading to a gradual slowdown in polarization growth and a quasi-saturation phenomenon. Additionally, the negative cubic coefficient e_2 introduces slight asymmetry, causing polarization enhancement in the negative displacement region to be slightly stronger than in the positive region.

In the K_3^{Append} mode (Fig. 3(d)), polarization exhibits a bipolar characteristic. Although the quadratic coefficient b_3 shows positive curvature, the negative quartic term d_3 competes with the positive sextic term f_3, resulting in a local maximum of polarization intensity around $Q_{K_3^{\mathrm{Append}}} \approx \pm 0.5$, which decreases at larger displacements. The cubic coefficient $c_3 = 0.549$ dominates the system's asymmetric response, while the quintic term e_3 further enhances the asymmetry. The near-zero linear term $a_3 \approx 0$ indicates that the polarization response is entirely nonlinear for the K_3^{Append} mode.

Within the range of in-plane lattice distortion in the smaller K_3 mode, the in-plane dielectric constant exhibits a significant nonlinear increase with the distortion variable, indicating a strong in-plane charge screening effect in the system. This strong screening suppresses the in-plane electric field ($\varepsilon_{\parallel} \gg 1$), thereby limiting further adjustment of the in-plane charge distribution. Constrained by this, the system achieves energy relaxation through out-of-plane charge redistribution, such as the asymmetric hybridization of the Mo atom's d_{z^2} orbital with the S/Se atom's p_z orbital, ultimately triggering a strong nonlinear dynamic polarization response.

The spatial gradient distribution of chalcogen elements exhibits significant non-reciprocal effects. For the K_2^{Append} mode, the out-of-plane displacement of the upper Se atoms ($\Gamma_1^{\mathrm{Ch},\perp}$) enhances interlayer charge transfer due to its larger atomic radius, partially offsetting the suppressive effect of the quartic term. In the K_3^{Append} mode, the antisymmetric displacement of the S atoms generates stronger electronic localization in the $Q > 0$ region due to its high electronegativity, leading to a significant asymmetric polarization response: when $Q > 0$, the positive cubic term contribution ($c_3 = 0.549$) partially cancels the suppressive effect of the quartic term; while for $Q < 0$, both terms synergistically accelerate polarization decay. This directional dependence of the electron-lattice coupling forms a vector addition effect with the intrinsic polarization P_0^{Janus} of the Janus structure.

Comparing the parameter changes between Tables 4 and 5, the chalcogen cooperative displacement alters the system's higher-order response characteristics: the quartic term coefficient of the K_2 mode changes from -0.614 (Mo displacement only) to -1.430, enhancing the nonlinear suppression at high displacement; while the sign reversal of the quadratic term in the K_3 mode indicates that chalcogen cooperative motion completely alters the polarization enhancement direction. This is attributed to the out-of-plane displacement of the Se atom, which reconstructs the charge transfer path, converting the in-plane motion that originally canceled the dipole moment into a polarization enhancement mechanism.

Overall, the synergistic displacements of chalcogen atoms in-plane ($K_i^{\mathrm{Ch},\parallel}$) and out-of-plane ($K_i^{\mathrm{Ch},\perp}$) affect the po-

larization P_z indirectly through higher-order terms, with their independent contributions being weak (linear terms $a_2, a_3 \approx 0$). Among them, $K_i^{\mathrm{Ch},\parallel}$ maintains in-plane motion with C_3 symmetry, altering Mo–S and Mo–Se bond lengths to modulate the d–p orbital hybridization strength, mainly contributing to the quadratic term coefficient b_i. $K_i^{\mathrm{Ch},\perp}$ induces an interlayer charge gradient, reflected in the significant value of the quartic term coefficient d_i. The chalcogen Γ mode ($\Gamma_1^{\mathrm{Ch},\perp}$) acts as an independent degree of freedom, participating in the potential-energy surface construction through various higher-order terms f_i, but its direct contribution to polarization intensity is negligible (linear term $a_i \approx 0$).

We therefore conclude that the switchable component of the out-of-plane polarization is dominated by ionic displacements, principally the relative vertical shifts of the S and Se sublayers, whereas electronic charge redistribution, although smaller in its direct contribution to ΔP, is crucial for reshaping the potential-energy surface (via changes in higher-order coefficients) and for stabilizing the ferroelectric double-well bistability.

Table 5. The value of each coefficient parameter in the phenomenological model of Eq. (5) in the absence of strain.

Coefficient	Value	Coefficient	Value
a_2	−0.027260	d_2	−1.429502
a_3	−0.000281	d_3	−1.935032
b_2	1.433001	e_2	0.187659
b_3	0.575620	e_3	−0.374617
c_2	−0.293105	f_2	0.555685
c_3	0.549083	f_3	0.994384

3.4. Phase transition dynamics and thermal stability analysis

To investigate the stability differences and phase transition behaviors between d1T$_S$- and d1T$_{Se}$-phase, we systematically conducted studies on the phonon spectrum and thermodynamic evolution. The supercell phonon spectra in Figs. 4(a) and 4(b) indicate that both phases exhibit no imaginary frequencies throughout the entire Brillouin zone, confirming their dynamical stability in the low-temperature ground state. Notably, the phonon branches of the 1T-phase in the low-frequency region (< 1 THz) show a slight dispersion softening, corresponding to the instability of Se atomic displacements, suggesting that Se atoms are susceptible to thermal fluctuation disturbances in high-temperature environments.

The evolution of polarization strength with temperature is obtained through first-principles molecular dynamics simulations (DFT-MD) combined with the charge center method (see Fig. 4(c)), with the temperature range set from 150 K to 550 K and a temperature interval of $\Delta T = 50$ K. By analyzing the polarization strength-temperature curve, the polarization difference ΔP between adjacent temperature points can be expressed as $\Delta P(T_i) = |P(T_i) - P(T_{i+1})|$. In the thermodynamic evolution process based on the d1T$_{Se}$-phase, the maximum polarization difference ($\Delta P = 0.24$ μC/cm^2) occurs between $T_i = 250$ K and $T_{i+1} = 350$ K. The Curie temperature is defined as the midpoint temperature of this interval, i.e., $T_c = \frac{250\ \mathrm{K}+350\ \mathrm{K}}{2} = 300$ K. Analysis shows that when the temperature rises to 300 K, the d1T$_{Se}$-phase undergoes significant structural reconstruction, specifically manifested as the cooperative displacement of Mo atom sublattices and out-of-plane collective motion of Se atomic layers. During this process, the system reconstructs into a zigzag chain structure with 1T′-phase characteristics through in-plane Peierls-like distortion, and as the temperature continues to rise, the polarization strength eventually stabilizes at 1.58 μC/cm^2.

This critical structural transformation behavior can be explained from the perspectives of collective free energy evolution and soft mode activation mechanisms. Although the thermal energy of a single atom at 300 K ($k_B T$) is smaller than the local potential barrier (≈ 0.03 eV; see Fig. S1 of the supporting information), in the actual system, many-body cooperative effects and local thermal fluctuations significantly reduce the effective free energy barrier. In other words, as the temperature increases, long-range fluctuations of the polarization order parameter and soft mode activation occur in the system, which leads to local excitations that cooperatively trigger the system to evolve along low-energy paths, ultimately achieving critical structural reconstruction. The NEB calculation (see Fig. S1 of the supporting information) indicates that the 1T′-phase is lower in energy (≈ 0.09 eV/f.u.) than the d1T$_{Se}$-phase, and that the lowest-energy 1T′ → d1T$_{Se}$ pathway has an energy barrier (≈ 0.12 eV/f.u.); together with the collective nature of the structural rearrangement, these results imply that formation of 1T′ is thermodynamically favored and that spontaneous reversion to d1T$_{Se}$ is kinetically suppressed under ambient conditions. It is noteworthy that the d1T$_S$-phase exhibits remarkable thermal stability, with its polarization intensity remaining at 1.78 μC/cm^2 at 550 K (a reduction of only 1.9% compared to 0 K), significantly outperforming the d1T$_{Se}$-phase. The enhanced robustness of the d1T$_S$-phase can be traced to stronger Mo–S bonding. Mo–S bonds are shorter and exhibit stronger d–p orbital hybridization, yielding larger (more negative) Integrated Crystal Orbital Hamilton Population (ICOHP) values (see Figs. S2 and S3 and the accompanying discussion of the supporting information). In contrast, the d1T$_{Se}$-phase, due to the larger atomic radius of Se, has longer bond lengths with Mo, leading to weaker orbital overlap and thus reducing d–p overlap and effective bond strength. This not only makes the release of stress in the local lattice easier at high temperatures but also promotes the Mo atoms to achieve structural reconstruction through in-plane displacements, thereby triggering a critical phase transition process in the system.

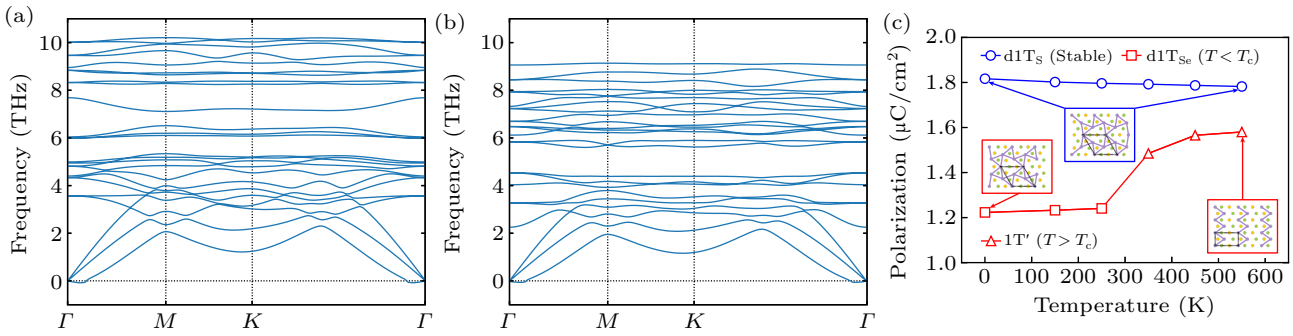


Fig. 4. (a) Phonon dispersion curves of the ferroelectric d1T_S-phase of monolayer MoSSe. (b) Phonon dispersion curves of the ferroelectric d1T_{Se}-phase of monolayer MoSSe. (c) Evolution of polarization with temperature for the d1T_S-phase (blue curve, stable over the entire temperature range) and the d1T_{Se}-phase (red curve), which undergoes a transition above $T_c \approx 300$ K. For the d1T_{Se}-phase, polarization exhibits a sharp increase after T_c, correlating with the formation of the 1T′-phase, characterized by zigzag chains of molybdenum atoms with Peierls distortion. Representative atomic structures at key temperatures are shown: d1T_S-phase indicated by a blue line box, d1T_{Se}-phase ($T < T_c$) indicated by a lower left red line box, and 1T′-phase ($T > T_c$) indicated by a lower right red line box.

4. Conclusion

This study systematically reveals the switchable polarization between two metastable polar states induced by symmetry breaking and their microscopic mechanism in Janus monolayer 1T-MoSSe, combining first-principles calculations with phenomenological models. The research finds that the inequivalent stacking of chalcogenide atomic layers (S/Se) breaks the central inversion symmetry of the system, activating the K-point phonon modes (K_2/K_3) that lead to a non-degenerate lattice instability. These two modes dominate the structural reconstruction of the d1T_S and d1T_{Se} metastable phases, and through the coupling of chalcogenide atomic cooperative displacements and charge redistribution, enable bipolar regulation of out-of-plane polarization strength ($\Delta P \approx \pm 0.3$ μC/cm^2). The Landau free energy model based on symmetry analysis indicates that the cubic anharmonic term and the inter-mode repulsive coupling together lead to an asymmetric double-well potential feature in the energy landscape, which is the key factor for the existence of bistable ferroelectricity.

Molecular dynamics simulations further reveal the thermodynamic competition between metastable phases: the d1T_S-phase remains stable with polarization ($P_z \approx 1.8$ μC/cm^2) at high temperatures (> 550 K), while the d1T_{Se}-phase undergoes an irreversible phase transition around 300 K, accompanied by a Peierls-like distortion of the Mo atomic chain and a jump in polarization intensity ($\Delta P \approx 24\%$). This difference in thermal stability arises from the gradient in electronegativity between S/Se atoms and is closely related to the effects of atomic radius and d–p orbital hybridization on bond length and binding energy. Specifically, the Mo–S bond, with its shorter bond length and more complete hybridization, has a higher chemical bonding energy, while the Mo–Se bond is relatively loose and more prone to phase transitions under thermal fluctuations.

This work not only predicts switchable polarization between bistable polar states in Janus-type transition metal chalcogenides for the first time, but also provides a theoretical framework for the design of nonlinear responses in two-dimensional ferroelectrics by constructing a polarization expansion model dependent on chalcogen displacement. The findings suggest that by controlling the competition between K_2/K_3 modes through strain or electric field, low-energy polarization reversal at room temperature can be achieved, which has potential significance for the development of non-volatile memory and piezoelectric sensors.

Acknowledgments

We gratefully acknowledge the financial support from the National Natural Science Foundation of China (Grant Nos. 12334014 and 11727902) and the Overseas High-level Talents Program of the Chinese Academy of Sciences.

References

[1] Birol T 2018 *Nature* **560** 174
[2] Novoselov K S, Mishchenko A, Carvalho A and Castro Neto A H 2016 *Science* **353** aac9439
[3] Yamauchi K and Barone P 2014 *J. Phys.: Condens. Matter* **26** 103201
[4] Lipatov A, Chaudhary P, Guan Z, Lu H, Li G, Crégut O, Dorkenoo K D, Proksch R, Cherifi-Hertel S, Shao D F, Tsymbal E Y, Íñiguez J, Sinitskii A and Gruverman A 2022 *npj 2D Mater. Appl.* **6** 18
[5] Lines M E and Glass A M 2001 *Principles and Applications of Ferroelectrics and Related Materials* (Oxford: Oxford University Press) pp. 14
[6] Watanabe Y 2010 *Ferroelectrics* **406** 35
[7] Shuai W J, Wang R and Zhao J Z 2023 *Phys. Rev. B* **107** 155427
[8] Liu F, You L, Seyler K L, Li X, Yu P, Lin J, Wang X, Zhou J, Wang H, He H, Pantelides S T, Zhou W, Sharma P, Xu X, Ajayan P M, Wang J and Liu Z 2016 *Nat. Commun.* **7** 12357
[9] Chang K, Liu J, Lin H, Wang N, Zhao K, Zhang A, Jin F, Zhong Y, Hu X, Duan W, Zhang Q, Fu L, Xue Q K, Chen X and Ji S H 2016 *Science* **353** 274
[10] Zhou Y, Wu D, Zhu Y, Cho Y, He Q, Yang X, Herrera K, Chu Z, Han Y, Downer M C, Peng H and Lai K 2017 *Nano Lett.* **17** 5508
[11] Cui C, Hu W J, Yan X, Addiego C, Gao W, Wang Y, Wang Z, Li L, Cheng Y, Li P, Zhang X, Alshareef H N, Wu T, Zhu W, Pan X and Li L J 2018 *Nano Lett.* **18** 1253
[12] Ding W, Zhu J, Wang Z, Gao Y, Xiao D, Gu Y, Zhang Z and Zhu W 2017 *Nat. Commun.* **8** 14956
[13] Xiao J, Zhu H, Wang Y, Feng W, Hu Y, Dasgupta A, Han Y, Wang Y, Muller D A, Martin L W, Hu P and Zhang X 2018 *Phys. Rev. Lett.* **120** 227601

[14] Sharma P, Xiang F X, Shao D F, Zhang D, Tsymbal E Y, Hamilton A R and Seidel J 2019 *Sci. Adv.* **5** eaax5080
[15] Fei Z, Zhao W, Palomaki T A, Sun B, Miller M K, Zhao Z, Yan J, Xu X and Cobden D H 2018 *Nature* **560** 336
[16] Yang Q, Wu M and Li J 2018 *J. Phys. Chem. Lett.* **9** 7160
[17] Sheng H, Fang Z and Wang Z 2023 *Phys. Rev. B* **108** 104109
[18] Shirodkar S N and Waghmare U V 2014 *Phys. Rev. Lett.* **112** 157601
[19] Choi J H and Jhi S H 2019 *J. Phys.: Condens. Matter* **32** 045702
[20] Yuan S, Luo X, Chan H L, Xiao C, Dai Y, Xie M and Hao J 2019 *Nat. Commun.* **10** 1775
[21] Wan L B, Xu B, Chen P and Zhao J Z 2023 *Phys. Rev. B* **108** 165430
[22] Zhou J, Wang Q, Sun Q, Chen X S, Kawazoe Y and Jena P 2009 *Nano Lett.* **9** 3867
[23] Guo Y, Zhou S, Bai Y and Zhao J 2017 *Appl. Phys. Lett.* **110** 163102
[24] Chen W, Hou X, Shi X and Pan H 2018 *ACS Appl. Mater. Interfaces* **10** 35289
[25] Yang Y, Zhang Y, Ye H, Yu Z, Liu Y, Su B and Xu W 2019 *Superlattices Microstruct.* **131** 8
[26] Wan X, Chen E, Yao J, Gao M, Miao X, Wang S, Gu Y, Xiao S, Zhan R, Chen K, Chen Z, Zeng X, Gu X and Xu J 2021 *ACS Nano* **15** 20319
[27] Zheng Z, Nottbohm C T, Turchanin A, Muzik H, Beyer A, Heilemann M, Sauer M and Gölzhäuser A 2010 *Angew. Chem. Int. Ed.* **49** 8493
[28] Lu A Y, Zhu H, Xiao J, Chuu C P, Han Y, Chiu M H, Cheng C C, Yang C W, Wei K H, Yang Y, Wang Y, Sokaras D, Nordlund D, Yang P, Muller D A, Chou M Y, Zhang X and Li L J 2017 *Nat. Nanotechnol.* **12** 744
[29] Hu T, Jia F, Zhao G, Wu J, Stroppa A and Ren W 2018 *Phys. Rev. B* **97** 235404
[30] Li S, Wu W, Feng X, Guan S, Feng W, Yao Y and Yang S A 2020 *Phys. Rev. B* **102** 235435
[31] Zhao J, Qi Y, Yao C and Zeng H 2024 *Phys. Rev. B* **109** 035408
[32] Er D, Ye H, Frey N C, Kumar H, Lou J and Shenoy V B 2018 *Nano Lett.* **18** 3943
[33] Yin W J, Wen B, Nie G Z, Wei X L and Liu L M 2018 *J. Mater. Chem. C* **6** 1693
[34] Dong L, Lou J and Shenoy V B 2017 *ACS Nano* **11** 8242
[35] Qiu J, Li H, Chen X, Zhu B, Guo H, Zhang F, Ding Z, Lang L, Yu J and Bao J 2021 *J. Appl. Phys.* **129** 125109
[36] Liu Z Q, Sun Z H, Qu X Y, Nie K K, Yang Y W, Li B J, Chong S K, Yin Z Y and Huang W 2024 *J. Am. Chem. Soc.* **146** 23252
[37] Yao Q F, Cai J, Tong W Y, Gong S J, Wang J Q, Wan X, Duan C G and Chu J H 2017 *Phys. Rev. B* **95** 165401
[38] Ma X, Wu X, Wang H and Wang Y 2018 *J. Mater. Chem. A* **6** 2295
[39] Zhang C, Nie Y, Sanvito S and Du A 2019 *Nano Lett.* **19** 1366
[40] Huang X H, Liu C S and Zhou P 2022 *npj 2D Mater. Appl.* **6** 51
[41] Kresse G and Furthmüller J 1996 *Phys. Rev. B* **54** 11169
[42] Kresse G and Hafner J 1993 *Phys. Rev. B* **48** 13115
[43] Perdew J P, Burke K and Ernzerhof M 1996 *Phys. Rev. Lett.* **77** 3865
[44] Perdew J P, Burke K and Ernzerhof M 1997 *Phys. Rev. Lett.* **78** 1396
[45] Zhang Y and Yang W 1998 *Phys. Rev. Lett.* **80** 890
[46] Henkelman G, Uberuaga B P and Jónsson H 2000 *J. Chem. Phys.* **113** 9901
[47] Henkelman G and Jónsson H 2000 *J. Chem. Phys.* **113** 9978
[48] Togo A and Tanaka I 2015 *Scr. Mater.* **108** 1
[49] Togo A 2023 *J. Phys. Soc. Jpn.* **92** 012001
[50] Togo A, Chaput L, Tadano T and Tanaka I 2023 *J. Phys.: Condens. Matter* **35** 353001
[51] Stokes H T, Hatch D M and Campbell B J 2007 *Isotropy software suite*
[52] Hoover W G 1985 *Phys. Rev. A* **31** 1695